

## Article

# Microstructural Evolution in Large-Section Plastic Mould Steel during Multi-Directional Forging

Xuan Chen , Boya Wu, Jiayuan Li, Xiaoxiao Zhang, Pengpeng Zuo, Xiaochun Wu and Junwan Li \* 

School of Materials Science and Engineering, Shanghai University, Shanghai 200444, China; chenxuan9311@163.com (X.C.); boya03@163.com (B.W.); lijiaoyuan\_0129@163.com (J.L.); zhangxx1020@163.com (X.Z.); zpp0513@163.com (P.Z.); wuxiaochun@shu.edu.cn (X.W.)

\* Correspondence: lijunwan@shu.edu.cn

**Abstract:** To obtain excellent mechanical properties from large cross-sections of plastic mould steel (SDP1), we conducted multi-directional forging (MDF) to control the microstructure of ingots. To investigate the microstructural evolution of SDP1 steel during MDF, we performed hot forging at 1150 °C using a THP01–500A hydraulic press. The dimensions of the specimens were  $\Phi 38$  mm  $\times$  80 mm. The microstructure of the specimens after forging was observed under a metallographic microscope. Furthermore, the results of the finite element method (FEM) simulations were employed to improve the quality of the forgings. The predicted results agreed well with the experimental ones, indicating that FEM is effective for analysing microstructural evolution during MDF. Thus, MDF for large cross-sections of SDP1 steel ( $\Phi 1000$  mm  $\times$  2200 mm) was simulated. The results showed that the average grain size of SDP1 steel at the core of an ingot after MDF ranged from 40.6 to 43.3  $\mu$ m. Although this was slightly higher than the grain size of the sample after traditional upsetting and stretching forging (TUSF) (35.7–46.0  $\mu$ m), the microstructure of the SDP1 steel sample after MDF was more uniform than that after TUSF. Compared with TUSF, MDF not only refines the grain size but also improves the microstructure uniformity of the sample.



**Citation:** Chen, X.; Wu, B.; Li, J.; Zhang, X.; Zuo, P.; Wu, X.; Li, J. Microstructural Evolution in Large-Section Plastic Mould Steel during Multi-Directional Forging. *Metals* **2022**, *12*, 1175. <https://doi.org/10.3390/met12071175>

Academic Editors: Shuwen Wen, Yongle Sun and Xin Chen

Received: 12 June 2022

Accepted: 8 July 2022

Published: 10 July 2022

**Publisher's Note:** MDPI stays neutral with regard to jurisdictional claims in published maps and institutional affiliations.



**Copyright:** © 2022 by the authors. Licensee MDPI, Basel, Switzerland. This article is an open access article distributed under the terms and conditions of the Creative Commons Attribution (CC BY) license (<https://creativecommons.org/licenses/by/4.0/>).

**Keywords:** multi-directional forging; large cross-section plastic mould steel; microstructure evolution; FEM simulation

## 1. Introduction

During the fabrication of large plastic mould steel blooms, the low impact toughness of the product is a major quality issue. Through microstructural analysis, this phenomenon is attributed to the coarse grain and nonuniform grain size [1–3]. As the most important manufacturing process for plastic mould steel, microstructural control in free forging processes determines product quality. Discontinuous dynamic recrystallisation (DRX), which occurs during hot deformation processes, is an important microstructural evolution behaviour. Recently, severe plastic deformation (SPD) methods have been widely studied owing to their ability to provide fairly good grain refinement in metallic alloys [4]. These techniques improve mechanical fatigue, corrosion, wear and creep properties of various alloys [5,6]. Several SPD methods, such as accumulative roll bonding, equal-channel angular pressing, friction stir processing and constrained groove pressing and multi-directional forging (MDF) [7–17], have found industrial applications. MDF has various advantages, such as repeatability, cost effectiveness, simplicity and the possibility of fabricating large parts [18–21].

MDF is a strong plastic deformation process improved by hammer forging compared with traditional unidirectional forming processes [22–25]. During MDF, the ingot is continuously elongated or compressed along the  $x$ -,  $y$ - and  $z$ -axes with changing loading direction, which has a great influence on the flow stress behaviour and the microstructure [26–28]. Although MDF of a large number of ferrous and nonferrous alloys have already been studied, there are few investigations on plastic mould steel available in the literature. For

example, Moghanaki et al. [24] studied the effect of solution treatment on the mechanical properties of Al-Cu-Mg alloy during multi-directional forging. The hardness of solution treated samples after MDF was strongly increased from 84 to 163 HV, which is attributed to both dynamic formation of Guinier-Preston-Bagaryatsky (GPB) zones/Cu-Mg co-clusters and dislocation storage. Nakao et al. [27], based on experiments on microstructure and mechanical properties, proved that the MDF can improve the level of grain refinement of stainless steel. In the process of MDF, the grain fragmentation degree increased due to the coordination of mechanical twins and martensitic transformation. With the increase in strain, the tensile strength significantly improved. Soleymani et al. [29] conducted multi-directional forging experiments on low-carbon steel modules and found that the grain refinement mechanism was static recrystallisation when the forging temperature was 500 °C. The new grains nucleated within the deformed grains, grew and consumed the deformed tissues until the material was completely recrystallised.

MDF has been studied and verified by many scholars, but in the manufacturing process of plastic mould steel, MDF technology has not been studied and applied. In this paper, both MDF and the traditional upsetting and stretching forging (TUSF) were carried out on the forging of large cross-sections of plastic mould steel. Based on the numerical simulation of the forging processes, the strain state and the evolutionary law of the microstructure during MDF and TUSF were investigated and discussed to provide effective guidance for the production of forgings.

## 2. Materials and Methods

### 2.1. Material

The material used in this study was as-forged micro-alloyed plastic mould steel (SDP1<sup>®</sup>), and its normal chemical composition is listed in Table 1. The steel sheet was manufactured by air and spray cooling after forging, and its thickness was 700 mm. The microstructure was observed and captured using an optical microscope (OM, Nikon, LV 150, Tokyo, Japan) and a field-emission scanning electron microscope (Carl Zeiss SUPRA 40, Oberkochen, Germany). For OM observation, the samples were mechanically ground using sandpaper, polished, and etched in a 4% nital solution.

**Table 1.** Normal chemical composition of SDP1 plastic mould steel (wt.%).

Element	C	Cr	Mn	Mo	Si	N	Nb	S	P	Fe
Wt.%	0.30	1.40	2.00	0.30	0.20	0.008	0.035	≤0.003	≤0.015	Bal.

### 2.2. MDF Procedure

Cylindrical samples (38 mm in diameter and 80 mm in length) were prepared by wire-electrode cutting, followed by homogenisation at 1150 °C for 2 h. MDF was performed to refine the grains of the SDP1 steel, and it was performed based on three-step forging (Figure 1a) using a THP01-500A hydraulic press (Tianduan, Tianjin, China). MDF was performed at an initial forging temperature of 1150 °C and a speed of 5 mm·s<sup>-1</sup> with a controllable deformation speed. During the process, the reduction was controlled at 50%. The ingots were reheated to 1150 °C for 0.5 h between every pass. In Figure 1a, P1 is located in the centre of the upper surface of the cylinder, P2 in the centre of the cylinder body, and P3 in the middle of the cylinder side surface. The samples were repeatedly deformed up to three passes by changing the loading direction in each pass by 90°. Prior to the second forging step, the pancake produced in the first step was rotated by 90° around the *x*-axis to press the *y*-plane of the ingot. The third forging process step was similar to the second step. Thus, the *z*-, *y*- and *x*-planes of the sample were compressed, in turn, to obtain fine grains. After the MDF process, to prevent the forged samples from cracking due to the rapid cooling, the ingots were pre-cooled until the temperature of the centre surface was below 850 °C, after which they were quenched in water. Samples 1–3 (Figure 1b) corresponded to the first, second and third steps of the forged ingots. To investigate the microstructure

of the MDF samples at different regions, three positions on the samples were selected for microstructural observation (Figure 1a). The samples were cut from the middle section of the forged billets. The middle area was representative of the entire sample and convenient for comparison. Austenite grain boundaries were shown by the oxidation method. The average grain size of the samples under different hot deformation positions was calculated based on the volume average of the grain using the three-circle truncated-point method. Several metallographic photographs were recorded at each sampling point to create grain size data statistics, and Image-pro Plus (version 6.0, Media Cybernetics, Rockville, MD, USA) was used to revise the data to obtain accurate and reliable average grain-size data.

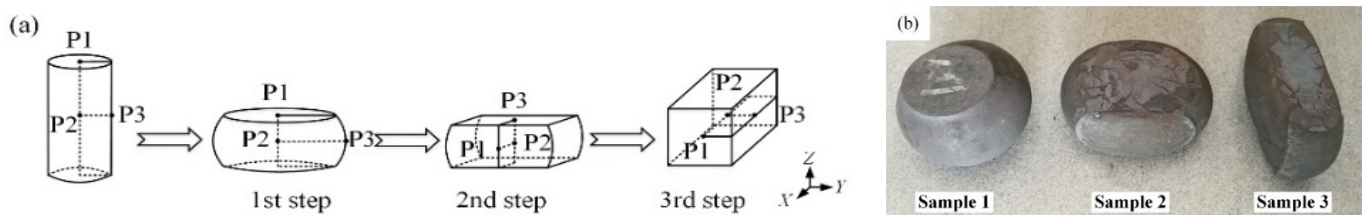


**Figure 1.** MDF experiment: (a) sequence of MDF steps; (b) state of SDP1 steel after MDF.

### 3. Experimental Results and Analysis

Figure 2 shows the grain size and morphology of the ingot before forging. The microstructure revealed fairly equiaxed grain morphology delineated with definite grain boundaries. The microstructure was characterised dominantly by coarse grains; the average grain size of the ingots was  $120\ \mu\text{m}$ , indicating coarse grains before the forging process. The ingots were collected from the hydraulic press after plastic deformation, but no crack was observed at the surface of the billets, suggesting that the alloy exhibited good workability at  $1150\ ^\circ\text{C}$ .

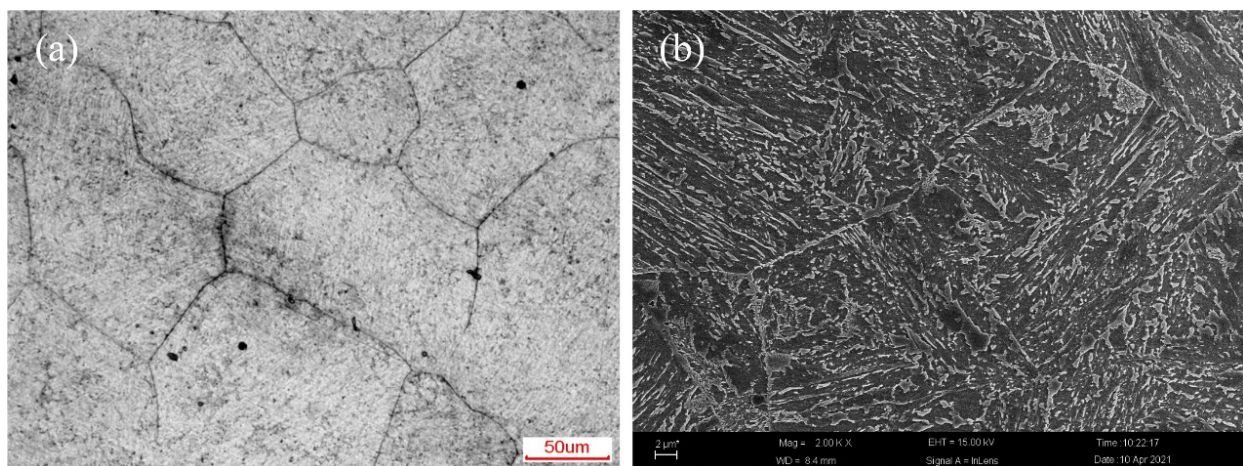


**Figure 2.** (a) initial grain size and (b) morphology of the SDP1 steel.

Figure 3 shows deformation microstructures of the samples after MDF, and Figure 4 shows the grain size distribution statistics of the SDP1 steel samples after MDF. The black area in the metallographic photographs shows an unpolished oxide layer, which does not affect the evaluation of the grain size. The grain size varied significantly with location during the MDF process (Figure 4a). Many deformed fine grains were observed in Sample 1, indicating recrystallisation during the MDF process. After the first step in the MDF process, many coarse grains were observed at point P1, and it was difficult to obtain more grain refinement. However, the grain size of points P2 and P3 decreased sharply. The average grain sizes of points P1, P2 and P3 of Sample 1 decreased from 120 to 119.0, 28.2 and 29.7  $\mu\text{m}$ , respectively. The MDF first step slightly affected the

average grain size of point P1, and more grain refinement could only be achieved by increasing the number of MDF passes. After the second step in MDF, the size distribution of point P1 showed significant refinement, and the distribution was dominated by 30–40  $\mu\text{m}$  grains (approximately 42.86%); in addition, grains in the range of  $<10\ \mu\text{m}$  and  $\geq 40\ \mu\text{m}$  constituted approximately 5.71% and 22.86%, respectively. After the third MDF step, the size distribution of point P1 was dominated by 20–40  $\mu\text{m}$  grains (approximately 70.73%), and grains  $\geq 40\ \mu\text{m}$  constituted only 2.44%.

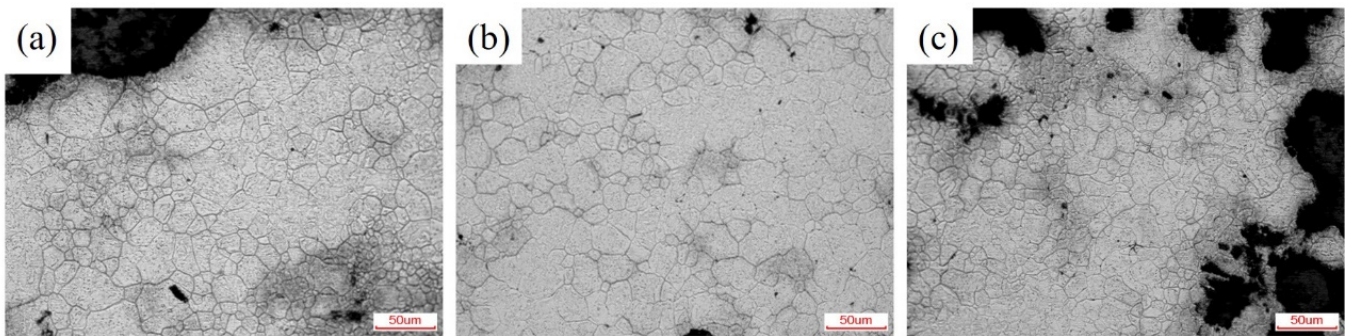


Figure 3. Microstructures of point P2 in (a) Sample 1; (b) Sample 2; (c) Sample 3.

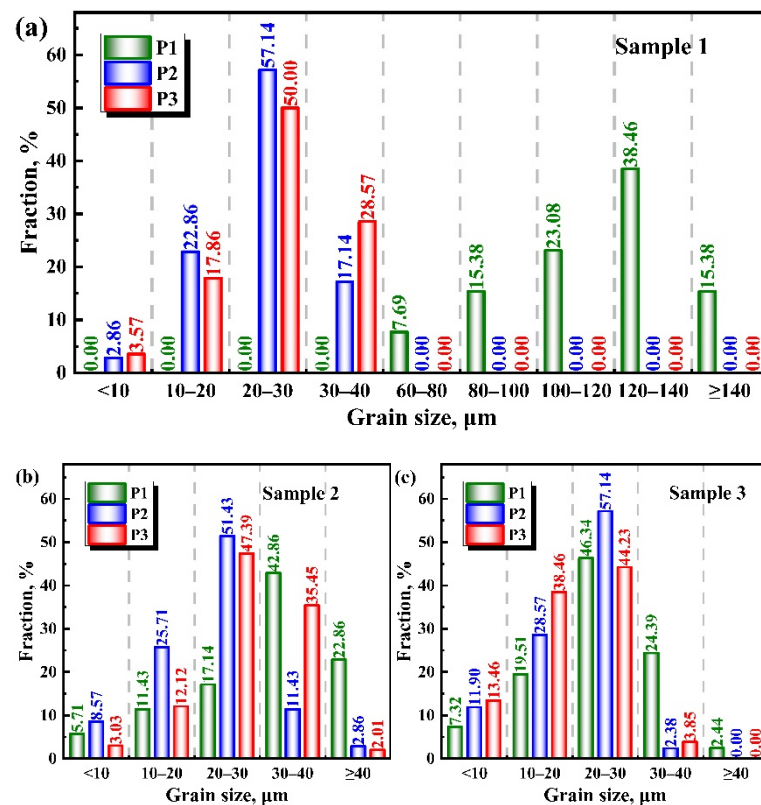


Figure 4. Grain size distribution and statistics of (a) Sample 1; (b) Sample 2; (c) Sample 3 at different tracking points.

All MDF steps resulted in remarkable grain refinement. With an increase in the MDF passes, the number fraction of the fine recrystallised grains increased (Figure 4b), and the recrystallisation grains became much finer than those obtained after one MDF pass. The grain size distribution of point P2 (Figure 4b) showed a broad distribution between 20 and 30  $\mu\text{m}$ , and the average grain size was 26.5  $\mu\text{m}$ . The number fraction of fine grains at point P2 increased compared with that of Sample 1. With a further increase in MDF passes, the

number fraction of fine recrystallised grains further increased (Figure 4c). A uniform fine grain structure evolved in Sample 3. The deformation microstructure was almost composed of mainly equiaxed fine grains considered to be recrystallisation grains. Homogeneous microstructures with average grain sizes of 28.7, 25.0 and 22.9  $\mu\text{m}$  were obtained at points P1, P2 and P3, respectively. Few grains larger than 40  $\mu\text{m}$  were obtained only at P1. The corresponding grain size distribution was characterised by a relative peak against the grain sizes ranging from 20 to 30  $\mu\text{m}$ . The number fractions of the grains ranging from 20 to 30  $\mu\text{m}$  in Sample 3 processed at points P1, P2 and P3 were 46.34%, 57.14% and 44.23%, respectively. The results show that MDF improved grain refinement. In addition to local coarse grains, the grains of the ingot were fine and uniform.

#### 4. Numerical Procedure

##### 4.1. Microstructural Evolution Model

Recrystallisation is a process by which deformed grains are replaced by new sets of grains that nucleate and grow until the original grains have been entirely consumed. Recrystallisation is important in developing microstructures in deformation-processed metals. Recrystallisation may occur during or after deformation; the former is termed dynamic, and the latter is termed static. The microstructure evolution model of SDP1 steel used in this simulation was derived from our previous calculations (Table 2) [30]. Combining the recrystallisation kinetic model and FE simulation of SDP1 steel, including the DRX, static recrystallisation (SRX) and meta recrystallisation (MRX), the effects of MDF and TUSF on the microstructural evolution of the ingots were investigated.

**Table 2.** Microstructural evolution model of SDP1 steel.

Quantity	Equation
Zener–Holloman parameter	$Z = 1.06 \times 10^{12} [\sinh(0.0094\sigma_p)]^{5.35}$
DRX grain size evolution	$D_{\text{DRX}} = 21400.5 \left[ \dot{\epsilon} \exp\left(\frac{257325}{RT}\right) \right]^{-0.26}$
DRX rate	$\epsilon_{0.5} = 0.0059 \dot{\epsilon}^{0.23} \exp\left(\frac{46187}{RT}\right)$
Peak strain	$\epsilon_p = 0.0011 \left[ \dot{\epsilon} \exp\left(\frac{257325}{RT}\right) \right]^{0.22}$
DRX fraction	$X = 1 - \exp\left[-0.693 \left(\frac{\epsilon - \epsilon_c}{\epsilon_{0.5} - \epsilon_c}\right)^2\right]$
Time for 50% SRX	$t_{0.5} = 4.5 \times 10^{-8} \epsilon^{-1.27} \dot{\epsilon}^{-0.25} \exp\left(\frac{151231}{RT}\right)$
SRX volume fraction	$X_{\text{SRX}} = 1 - \exp\left[-0.693 \left(\frac{t}{t_{0.5}}\right)^{1.1}\right]$
Time for 50% MRX	$t_{0.5} = 1.22 \times 10^{-6} \dot{\epsilon}^{-0.41} \exp\left(\frac{126605}{RT}\right)$
MRX volume fraction	$X_{\text{MRX}} = 1 - \exp\left[-0.693 \left(\frac{t}{t_{0.5}}\right)^{0.6}\right]$
Grain growth	$d_g^{8.18} = d_0^{8.18} + 6.03 \times 10^{54} t \exp\left(\frac{-800866}{RT}\right)$

$\sigma_p$ —peak stress, MPa;  $\epsilon$ —strain;  $\dot{\epsilon}$ —strain rate;  $\epsilon_c$  and  $\epsilon_{0.5}$ —critical strain rate and the DRX rate;  $R$ —gas constant, 8.314 J mol<sup>−1</sup> K<sup>−1</sup>;  $T$ —deformation temperature, K;  $t$ —time, s;  $d_0$ —initial grain size,  $\mu\text{m}$ .

##### 4.2. FEM Model

A comparative experiment was conducted to verify the accuracy of the recrystallisation model. To compare with the hot compression test, a cylindrical ingot ( $\Phi 38 \text{ mm} \times 80 \text{ mm}$ ) was used for MDF. The speed of the press was approximately 5 mm s<sup>−1</sup>. During MDF, the height of the ingot after each pass was reduced to 40, 27 and 35 mm along the  $z$ ,  $y$  and  $x$  central axes of the ingot, respectively.

As shown in Figure 5, a hexahedron element was used to discretize the ingot during FEM simulations. The suitable mesh ensured simulation precision and saved computing resources. The as-homogenised SDP1 steel had an average grain size of 120  $\mu\text{m}$ . Based on the experimental data, the average initial grain size of the ingot was set to 120  $\mu\text{m}$ , and other simulation parameters were also consistent with the experimental values. Combining

the recrystallisation kinetic model and the FEM of SDP1 steel, the effects of MDF on the microstructural evolution in forgings were simulated.

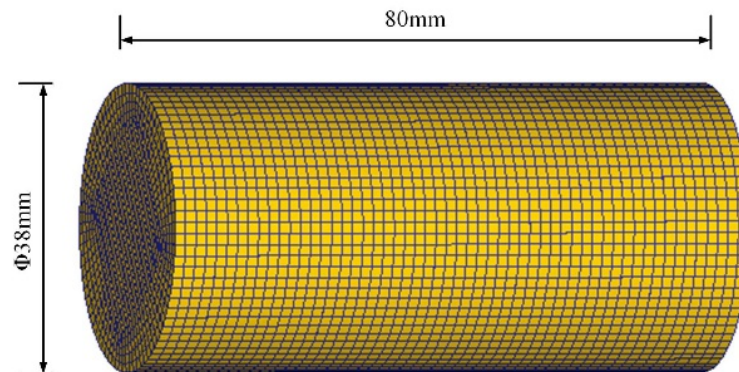


**Figure 5.** Three-dimensional finite element (FE) model of the specimen.

Microstructural evolution is not a major concern in the FE simulation of hot forging; thus, hot forging numerical theory only considers the coupling effect of the temperature and stress/strain fields. The coupling effect between the temperature and stress/strain evolution is described as follows. On the one hand, the plastic-deformation work accumulated in forging is converted into an internal heat source at a certain proportion. On the other hand, because of the existence of a temperature gradient, the expansion is different. Finally, a thermal strain is induced.

The instantaneous temperature field of the forging blank in a forging process can be expressed by the Fourier heat-transfer equation in a rectangular coordinate system.

$$\frac{\partial}{\partial X}(\lambda \frac{\partial T}{\partial X}) + \frac{\partial}{\partial Y}(\lambda \frac{\partial T}{\partial Y}) + \frac{\partial}{\partial Z}(\lambda \frac{\partial T}{\partial Z}) + \frac{\partial Q_2}{\partial t} = \rho c \frac{\partial T}{\partial t} \quad (1)$$

where  $X$ ,  $Y$  and  $Z$  are the three directions of the rectangular coordinate system;  $\rho$ ,  $c$  and  $\lambda$  are the density, specific heat capacity, and thermal conductivity of the materials, respectively; and  $Q_2$  and  $t$  are the internal heat source and time, respectively. The change rate of the heat source can be expressed as follows:

$$\frac{\partial Q_2}{\partial t} = \dot{q} = kq \cdot \bar{\sigma} \cdot \dot{\bar{\epsilon}} \quad (2)$$

where  $kq$  is the conversion ratio of the heat-to-plastic deformation work;  $\bar{\sigma}$  is the effective stress;  $\dot{\bar{\epsilon}}$  is the effective strain rate. This equation realizes unilateral coupling of the stress/strain field to the temperature field.

Initial and boundary conditions must be determined to solve the transient-heat-conduction problem. The initial temperature of the forging blank was uniform and not less than 1150 °C. It can be expressed as:

$$T(X, Y, Z)|_{t=0} = T_0(X, Y, Z) \quad (3)$$

The boundary condition of the forging blank can be divided into two categories depending on whether the forging blank is in contact with the die. The boundary condition of a free surface that is not in contact with the model is expressed as follows:

$$qf = Hf(T_f - T_E)(S \in Sf) \quad (4)$$

where  $S$  is the module surface;  $Sf$  is a free surface;  $q_f$  and  $T_f$  are the heat flow and temperature of the free surface, respectively;  $T_E$  is the environment temperature;  $Hf$  is the total heat-transfer coefficient including convection and radiation heat transfer. Thus, the boundary condition of the free surface belongs to the second boundary condition.

For the surface in contact with the die, the heat-transfer mechanism was very complex, which can be roughly divided into the following two heat-transfer mechanisms. On the one hand, heat conduction was achieved through the contact points between the blank and anvil and solid interstitials (oxide skin, etc.). In addition, the friction heat generation between the die and forging blank should be considered. Thus, the boundary condition of the contact surface can be written as:

$$q_c = H_c(T_c - T_d) + q_\mu(S \in S_c) \quad (5)$$

where  $S_c$  represents the contact surface;  $q_c$  and  $q_\mu$  are the total and friction heat flows of the contact surface, respectively;  $H_c$  denotes the total heat-transfer coefficient of the contact surface;  $T_c$  and  $T_d$  are the temperatures of the contact and die surfaces, respectively.

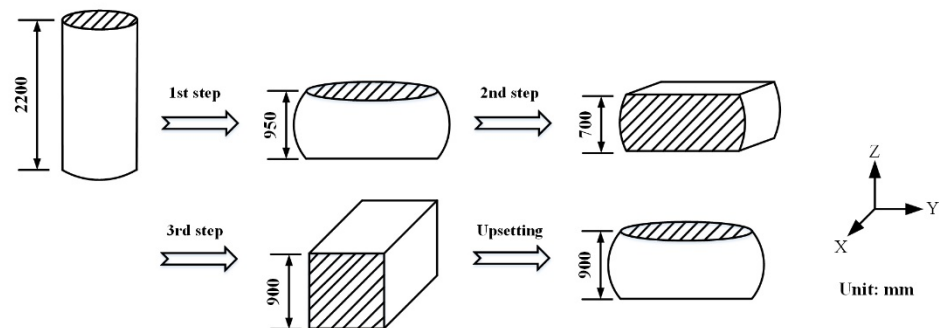
The stress/strain field of hot forging satisfies the assumption and basic equation of a rigid-plastic material. In addition, we need to specify the coupling effect of the temperature field on the stress/strain field.

$$\Delta \varepsilon^T = \alpha_2(\Delta T) \quad (6)$$

where  $\varepsilon^T$  and  $\Delta T$  are the thermal strain and temperature increments, respectively;  $\alpha_2$  is the thermal expansion coefficient of the forging blank.

The forging blank is cylindrical with dimensions of  $\Phi 1000 \text{ mm} \times 2200 \text{ mm}$  (Figure 6). Because the forging blank is formed in different directions, instead of simplifying the model using a symmetrical relationship, we used the entire model. The geometry of the forging blank was meshed using a hexahedral element, and more than 10,000 hexahedral elements were obtained. To simulate the heat transfer between the forging blank and the mould, meshing the forging blank is insufficient; thus, a discrete mould geometry was employed.

(a) Multi-directional forging (MDF)



(b) Traditional upsetting and stretching forging (TUSF)

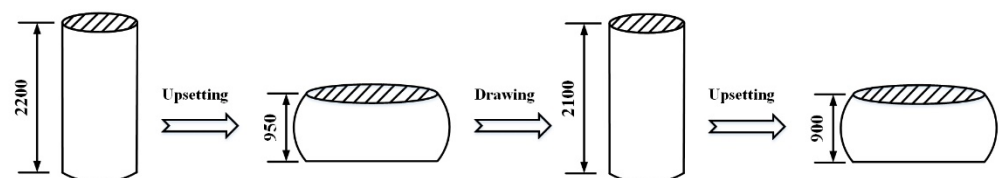


**Figure 6.** Schematic of (a) MDF and (b) traditional upsetting and stretching forging (TUSF) processes.

Furthermore, TUSF was conducted to compare with MDF. In these two forging processes, the first step was to upset the  $z$ -direction. Thus, the forging blank height could be forged from 2200 to 950 mm. In the second TUSF step, the blank was forged in the  $y$ -direction using a small smith anvil, and the height was reversed to 2200 mm. In the drawing process, the feed and reduction rates were maintained at 50% and 25%, respectively. In the second and third MDF steps, the blank was forged to 700 and 900 mm in the  $y$ - and  $x$ -direction, respectively, by successively using a large Smith anvil. A TUSF pass consisted of upsetting and elongation in the  $z$ - and  $y$ -directions, respectively, whereas one MDF pass

involved upsetting in the  $z$ -direction and compression in the  $y$ - and  $x$ -directions. Finally, the MDF and TUSF samples were upset to a height of 900 mm. Thus, TUSF and MDF differ in terms of the steps after  $z$ -direction upset. Upset in the  $z$ -direction has attracted attention because it is the first step and results in maximum deformation.

For both TUSF and MDF, a compressive speed of 10 mm/s was adopted. The friction and heat transfer coefficients of the anvil and blank were 0.3 and 11, respectively. The initial temperature of the forging blank was 1150 °C, and the temperature of the anvil and the ambient temperature were 150 °C and 20 °C, respectively. Before each step, the temperature of the blank was reset to 1150 °C. Based on the austenite grain size in the high-temperature homogenisation state, the average initial grain size of the ingot was set to 200  $\mu\text{m}$ . Combining these two forging procedures and the FE model of hot forging, we simulated two-pass TUSF and MDF to analyse the distribution of temperature, effective stress and effective strain in the forging blank.

## 5. Results and Discussion

When the sample was compressed with a flat anvil, the metal flew around as the height decreased because of the friction between the specimen and the anvils, making it difficult for the metal to deform near the contact surface. Thus, the compressed specimen formed a drum shape, resulting in different grain sizes at different positions on the specimen. During the first MDF step (i.e., upsetting), the deformed specimen is divided into three regions (Figure 7). Region I is located near the interface between the specimen and the anvils, which is greatly affected by friction, reducing plastic deformation [25]. Region II is far from the end surface and is subject to less friction. It is in the most favourable deformation area at an angle of 45° to the vertical force and prone to plastic deformation. Region III is a small deformation zone, which is close to the surface of the specimen and around region I, and the extent of deformation is between that in regions I and II.

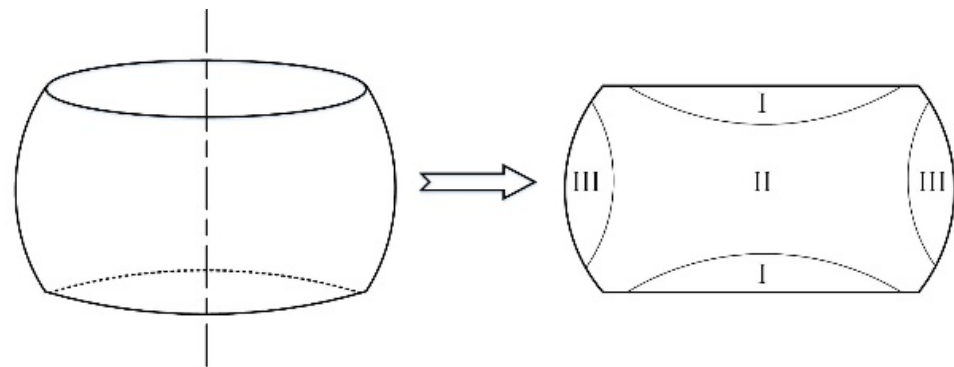


**Figure 7.** Schematic of difficult (I), large (II) and small (III) deformation areas of the specimen after upsetting.

### 5.1. Comparative Analysis of Experimental and Simulation Results

Figure 8 shows the experimental and simulated specimens after MDF. The arrows in Figure 8a–c indicate the flow state of the material during plastic deformation. Comparing the two sets of data, we find that FEM could well predict the shape and size of deformation forgings, which can guide the forging process. Figure 9 shows the average grain size distribution of the specimen after different forging steps. The samples show regular shapes after different forging steps, and a drum shape was formed on the side of each sample, which was similar to the shape of the ingot used in the experiment. Figure 9a shows the grain size distribution after the first step of MDF. Compared with Figure 4, the average grain size near the interface was quite large. The grain size near the centre of the interface (i.e., point P1) was the largest (119  $\mu\text{m}$ ), which is consistent with the initial grain size without refinement. The core of Sample 1 had the smallest grain size of 24.2  $\mu\text{m}$ . The grain size of point P3 was close to but not as uniform as that of point P2. After MDF,

the grain of Sample 3 was tiny and distributed uniformly. For some areas with uneven grain distribution, secondary forging or other heat-treatment processes can be carried out. The simulation results were in good agreement with the experimental results. The FEM simulation results showed that the evolutionary law of the average grain size can well reflect the microstructural evolution of recrystallisation. Meanwhile, FEM is an effective method for analysing the thermal compression process, and the obtained recrystallisation model of SDP1 is reliable and effective.

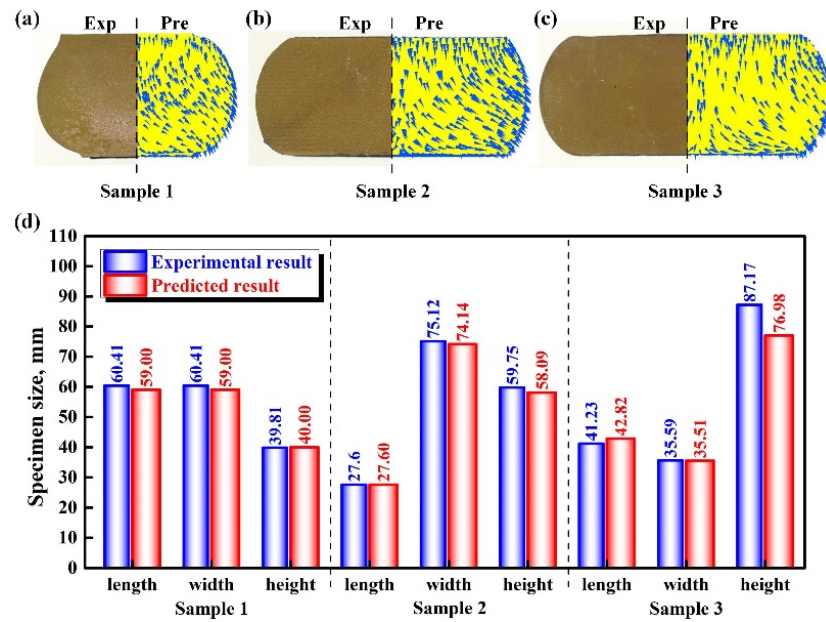


Figure 8. Experimental and simulated specimen sizes after MDF. (a) sample 1, (b) sample 2, (c) sample 3, (d) three-dimensional comparison.

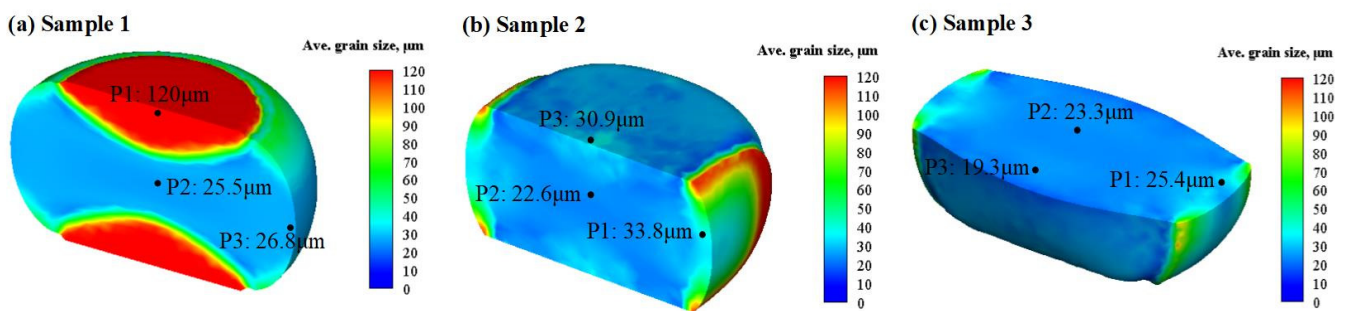
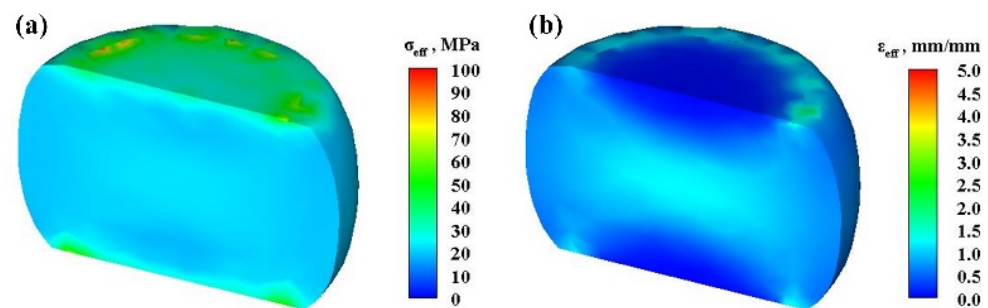


Figure 9. Average grain size of (a) Sample 1; (b) Sample 2; (c) Sample 3 at different tracking points obtained from FEM results.

### 5.2. Microstructural Evolution during the First MDF Step

Figure 10 shows the effective strain and stress contour plots of the deformed specimen after MDF at 1150 °C. The results show an inhomogeneous distribution of effective strain in the samples during MDF. The nonuniform strain distribution after upsetting agreed with the characteristics of the three deformation zones in the specimen. The accumulated strain in region I was higher than that in the other two regions. During upsetting, the strain distribution was extremely uneven, and the strain value decreased gradually from the centre along the radius to the side surface. In region I, where the specimen was in contact with the anvils, due to the friction resistance and heat transfer, the deformation was very small, because the magnitude of friction varied inversely with the distance, and region I was a cone. The outer drum part of region III was a free surface, which was less affected by friction resistance and depended on the expansion of region I; thus, longitudinal bulging was observed. With the same reduction, the deformation decreased from the centre to the end face. The maximum effective strain inside the sample reached 1.78, and the minimum effective strain was 0.03 after upsetting.



**Figure 10.** (a) Effective stress and (b) strain distributions of specimens after upsetting.

Grain refinement due to the fact of recrystallisation during the forging process determines the final grain size of an alloy. As shown in Figure 11a, the uneven distribution of deformation resulted in a difference in grain size in different regions. The as-homogenised coarse grain structure underwent significant grain refinement during the upsetting process. The recrystallisation volume fraction of region I was small because of the small strain, and there was no recrystallisation at the centre of the region. The grain size of the region was the same as the initial grain size, and recrystallisation occurred only in some regions. Due to the severe deformation in region II, there was adequate recrystallisation in the region, the grain size was uniform, and the centre of the region was completely recrystallised. The grain size of region III was not uniform, unlike in regions I and II. Compared with other regions, region II showed the largest deformation and the most sufficient recrystallisation. Compared to the edge region, the accumulated strain at the centre was larger, and recrystallisation occurred at the initial stage of the MDF process, providing more potential sites for recrystallisation nuclei. A higher accumulated strain indicates higher stored energy and an increased driving force for recrystallisation [31]. Consequently, a finer and more homogeneous grain structure was formed at the centre region after upsetting. In addition, due to the heat transfer between the specimen and the dies and that between the specimen and the environment, the final temperature around the specimen was much lower than that of the specimen core after upsetting. Consequently, finer and more homogeneous grain with an average grain size range of 45.7–49.9  $\mu\text{m}$  developed at the centre region after upsetting.

Recrystallisation is a process that can induce stress relaxation to varying extents in a deformed metal by releasing the stored energy arising from the deformation process when heat-treated at an appropriate temperature [32]. Recrystallisation is important in microstructural development in deformation-processed metals [33]. During upset simulation, three types of recrystallisation behaviour, including DRX, SRX and MRX, may occur within

the sample. DRX occurs during high-temperature deformation, and it aids grain refinement and homogenisation. Figure 11b shows that the DRX volume fraction in region II was sufficient for grain refinement. The DRX fraction at the core of the sample reached 100%, and the grains were uniformly distributed. The microstructure agreed with the stress–strain field. SRX occurs in high-temperature multi-pass deformation gaps of materials. MRX differs from SRX. It occurs with DRX at the core and continues to grow within the gap time. As shown in Figure 11c,d, neither SRX nor MRX occurred during upsetting. This was because upsetting was a one-off finish, and there was no time for deformation gaps. Thus, it cannot provide sufficient conditions for SRX or MRX [34–40].

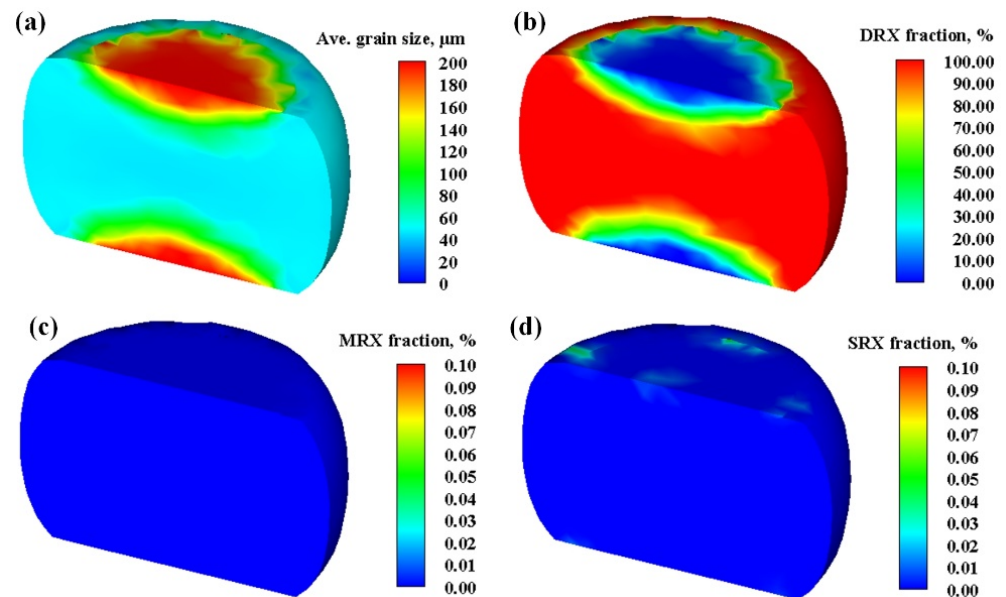


**Figure 11.** (a) Average grain size; (b) dynamic recrystallisation (DRX); (c) meta-recrystallisation (MRX); (b,d) static recrystallisation (SRX) fractions in the specimen after upsetting.

To further investigate the grain evolution, different points on the specimen were observed as shown in Figure 12a. With an increase in reduction during the MDF process, both the effective strain at the centre (P2) and side (point P3) regions increased, and the difference in the accumulated strain between the centre and side regions increased, but there was a little change in the effective strain at P1. After upsetting, the effective strain at points P1, P2 and P3 were approximately 0.03, 1.24 and 0.72, respectively. The average grain sizes at points P2 and P3 decreased as the reduction exceeded a certain value (Figure 12c). Point P2 recrystallised in 17 s, which was earlier than that at P3 (18 s), and the rate of grain refinement at P2 was greater than that at P3. Compared with P3, P2 showed a better grain refinement effect, and the final average grain size was obtained first. In contrast, P1 was restricted by friction resistance, the strain was always lower than the critical strain, and no recrystallisation occurred. The final average grain size at P1, P2 and P3 was 200, 45.4 and 45.6  $\mu\text{m}$ , respectively. The DRX volume fractions at P2 and P3 (Figure 12d) increased when the reduction exceeded a certain value, which is consistent with Figure 12b,c. At 17 s, that is, when the strain reached 0.15, the recrystallisation fraction at P2 increased first. Complete recrystallisation occurred at P2 and P3 after upsetting, but no DRX occurred at P1, which is in a difficult deformation zone. The final DRX fractions at P1, P2 and P3 were 0%, 100% and 100%, respectively.

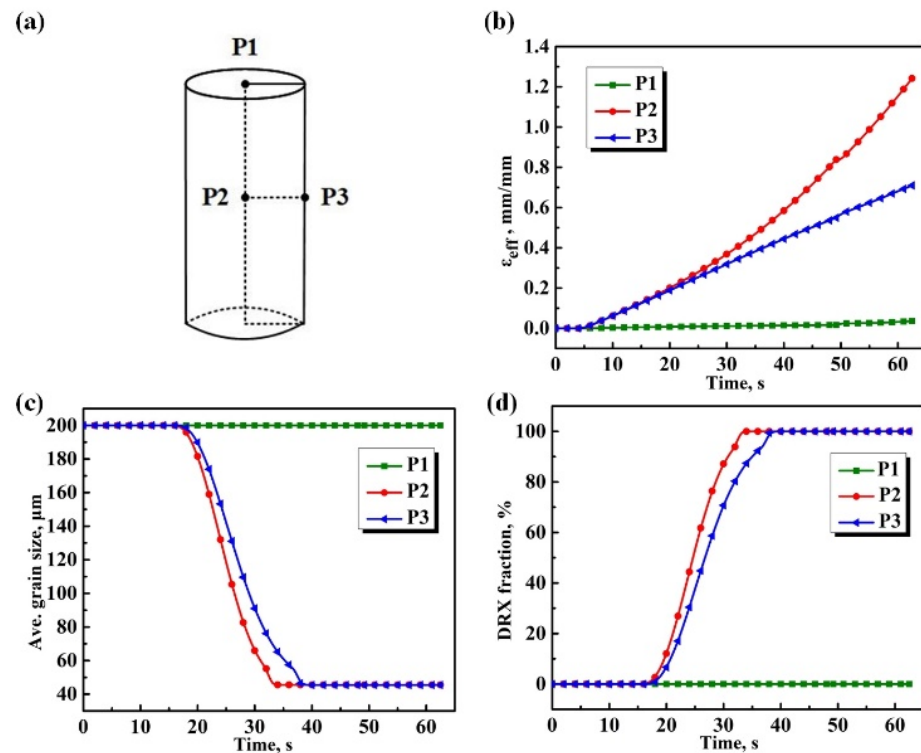


**Figure 12.** (a) Different tracking points; (b) effective strain; (c) average grain size; (d) DRX fraction curves.

### 5.3. Comparison of Microstructural Evolution between MDF and TUSF

Drawing is a forging process in which the cross-sectional area of a blank is reduced, and the length is increased by deformation. According to the strain during each compression deformation, drawing increases the length through continuous accumulation of axial strain. The end surface of the specimen was in contact with an anvil; thus, it was affected by friction resistance, resulting in limited deformation and smaller strain at the region. On the other hand, friction resistance decreased towards the specimen centre, resulting in more deformation at the centre (Figure 13). Herein, the maximum and minimum strains after MDF were 3.86 and 0.6, respectively. Compared with MDF, the feeding amount of each drawing step was small in TUSF, and it was necessary to rotate the specimen to achieve deformation. Therefore, the TUSF process was more complex and inefficient. After TUSF, the maximum and minimum strains were 3.43 and 0.32, respectively.

The average grain size varied from 40.6 to 43.3  $\mu\text{m}$  at the centre of the specimen after MDF (Figure 14a) and from 35.7 to 46.0  $\mu\text{m}$  after TUSF (Figure 14b). The average grain size of the specimen core after TUSF was slightly smaller, but the range was higher than that of the sample after MDF. The DRX of MDF was more adequate, and the grain at the centre was more uniform; meanwhile, the surface of the sample was neater after MDF than after TUSF. The minimum and maximum grain sizes were 1 and 60  $\mu\text{m}$ , respectively after MDF. However, the surface of the sample after TUSF was not smooth. The minimum and maximum grain sizes were 12 and 132  $\mu\text{m}$ , respectively. The large span of the grain size and incomplete recrystallisation in the local region after upsetting and drawing affected the comprehensive performance of forging and, subsequent, processing. The SRX and MRX volume fractions of the MDF ingot were much lower than those of traditional forging, because MDF is a continuous compression deformation process. The ingot showed DRX during deformation, and the DRX fraction in most regions of the ingot reached 100%. In contrast, the conditions were provided for SRX and MRX during the TUSF process. In general, grain refinement was mainly achieved by DRX; grain refinement and dynamic softening caused by the SRX and MRX were relatively low.

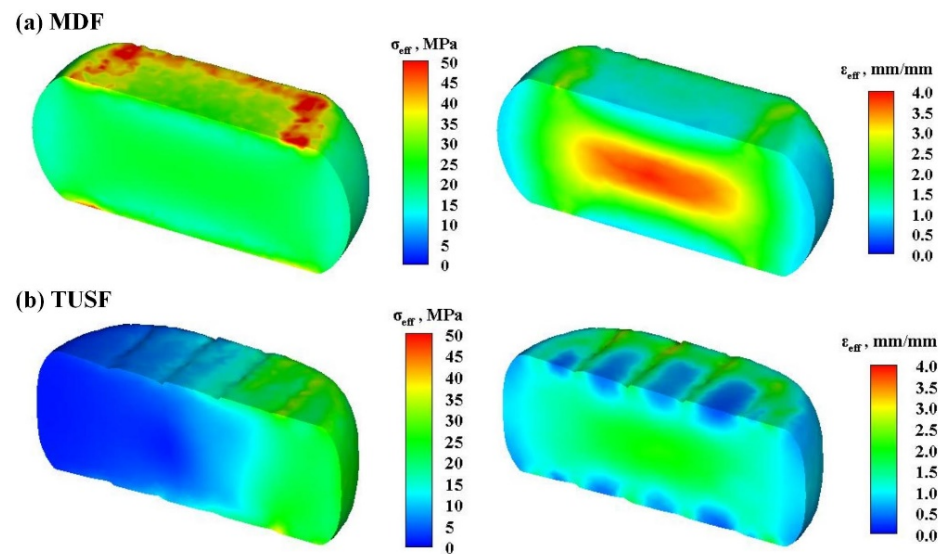


Figure 13. Effective stress and strain distributions of specimens after (a) MDF and (b) TUSF.

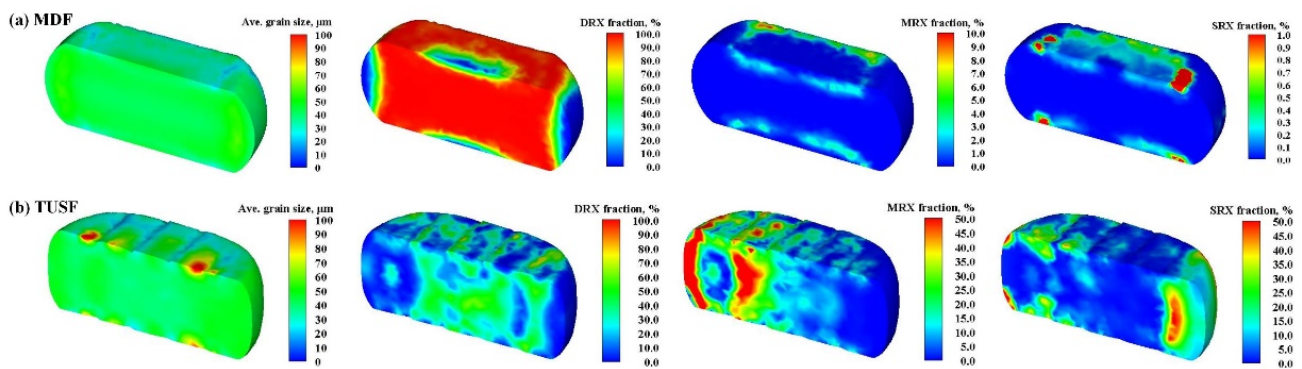


Figure 14. Schematic diagram of the microstructural distribution and recrystallisation behaviour after (a) MDF and (b) TUSF.

Second upsetting deformation was carried out after a complete MDF and TUSF to compare and analyse the effects of MDF and TUSF on subsequent deformation of ingots. Due to the influence of friction resistance on the end surface of the specimen, the nonuniform deformation of the specimen showed a drum shape. The distribution of effective stress and strain was consistent with the characteristics of the three deformation regions in the upsetting process (Figure 15). As shown in Figure 16, with an increase in reduction, strain at the three points increased gradually and reached a maximum. The initial effective strains at P1, P2 and P3 in the MDF sample were 0.86, 3.89 and 1.88, respectively, and the final strains were 1.15, 5.02 and 2.10, respectively. The initial values at P1, P2 and P3 in the TUSF sample were 0.91, 2.07, 1.18, and the final strain values were 1.07, 3.18 and 1.63, respectively.

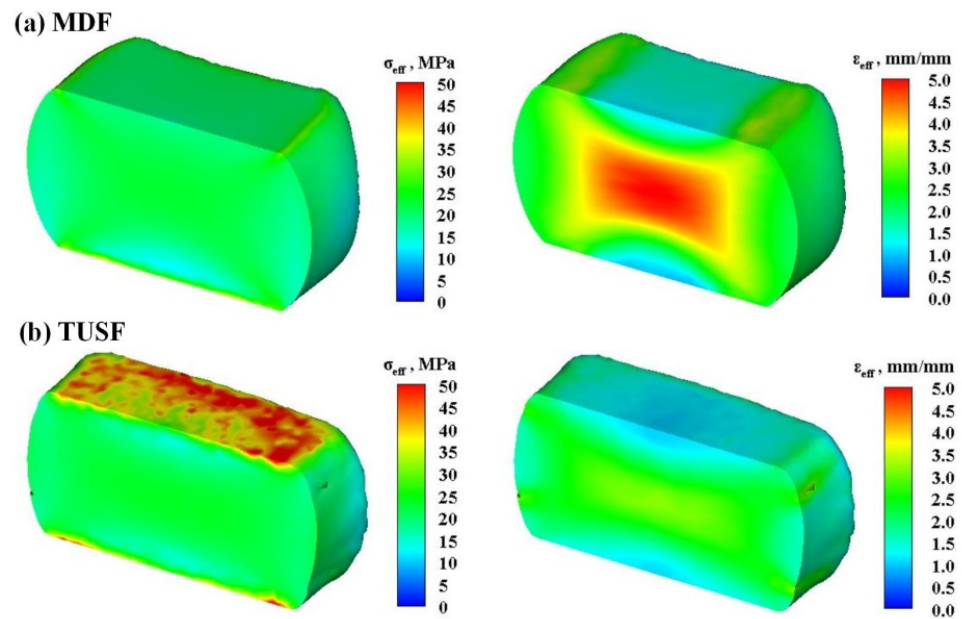


Figure 15. Effective stress and strain distributions in (a) MDF and (b) TUSF specimens.

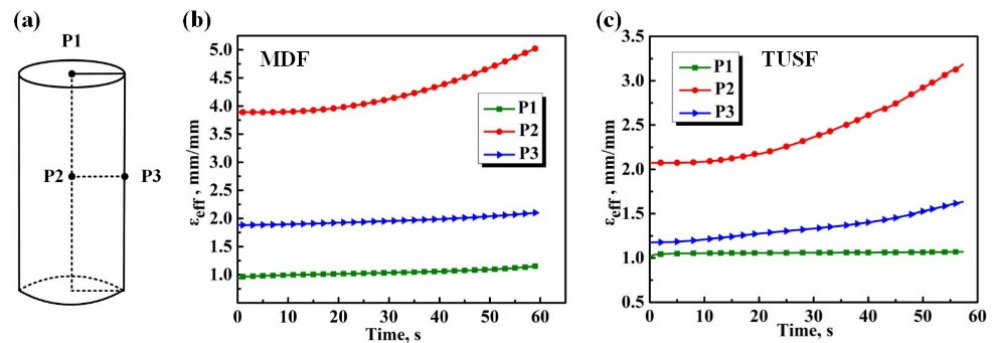
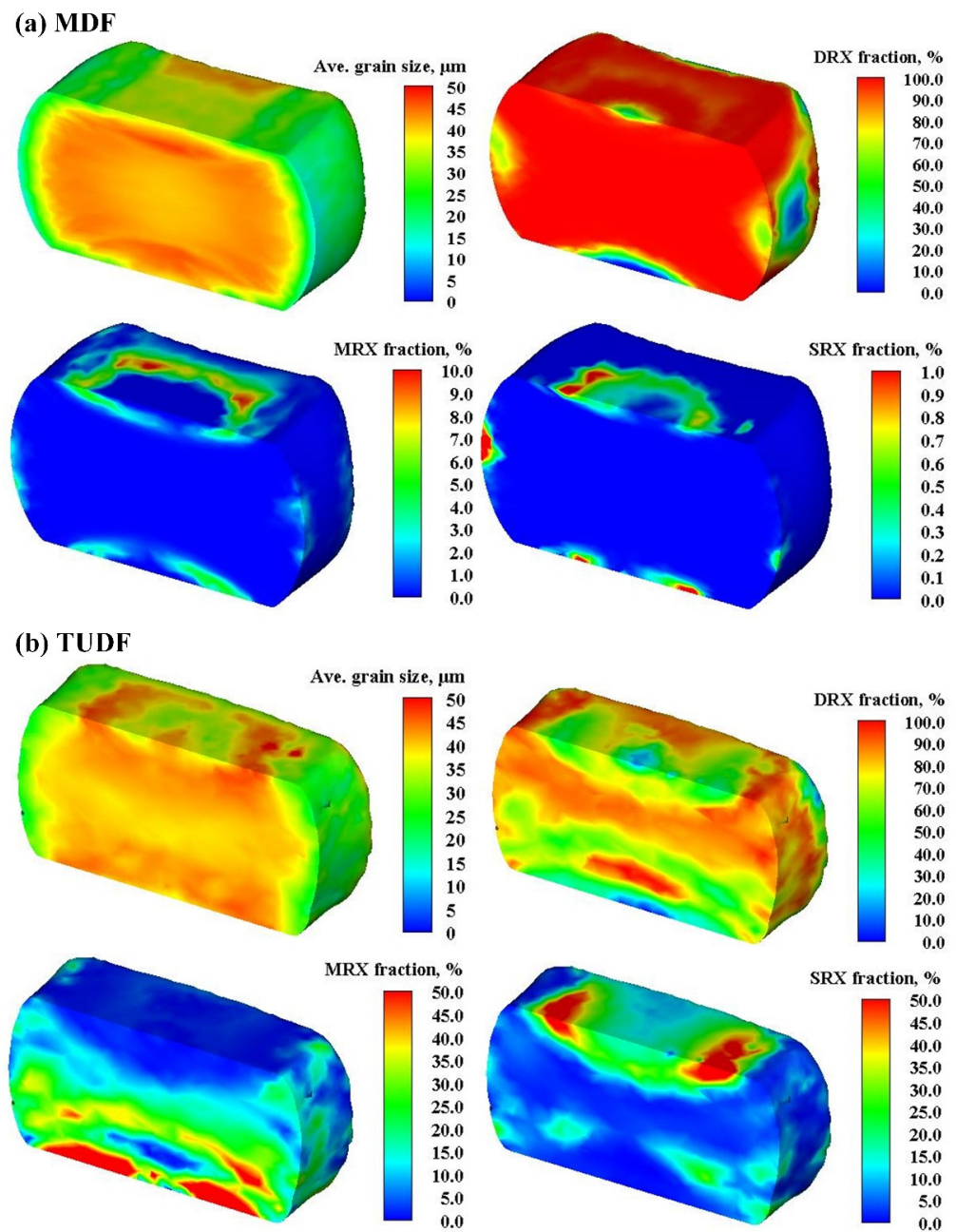


Figure 16. Time-dependent effective strain curves for (b) MDF and (c) TUSF specimens at (a) different tracking points.

The average grain size ranged from 40.2 to 41.8  $\mu\text{m}$  in the core of the MDF specimen and from 38.7 to 42.2  $\mu\text{m}$  in that of the TUSF specimen. Their average values were similar. The grain size in the core of the TUSF specimen was slightly smaller, but the range was slightly higher. Analysing and comparing Figure 17a,b, we can find that DRX in the MDF sample was more sufficient. The recrystallisation volume fraction in the core of the MDF specimen reached 100%, and the grain size was more uniform than that of the TUSF specimen. The minimum and maximum grain sizes of the entire sample were 12 and 52  $\mu\text{m}$ , respectively. However, the surface of the TUSF specimen was not smooth, and the minimum and maximum grain sizes were 13 and 63  $\mu\text{m}$ , respectively. The grain size of a traditional forging specimen was large, the grain of the sample centre was not uniform and there were mixed crystals, which can affect the overall performance of forged samples and subsequent processing.



**Figure 17.** Microstructural distribution contours for the (a) MDF and (b) TUSF specimens.

The initial grain sizes at P1, P2 and P3 in the MDF specimen were 39, 40 and 17  $\mu\text{m}$ , and the final grain sizes were 36, 40 and 14  $\mu\text{m}$ , respectively (Figure 18). The grain size at P2 was almost unchanged, and that at P1 and P3 decreased significantly, possibly because the deformation on the side surface was relatively large, and the grains on the surface were easily broken. However, the temperature of the core remained at the initial temperature of 1150  $^{\circ}\text{C}$ , the grain plasticity was good, and the grains would not fracture during plastic deformation. On the other hand, the initial grain sizes at P1, P2 and P3 on the TUSF specimen were 46, 39 and 41  $\mu\text{m}$ , and the final grain sizes were 42, 39 and 24  $\mu\text{m}$ , respectively. After further treatment, the grain structure at P2 remained unchanged, and the average grain size was 39  $\mu\text{m}$ . There are more variations in the average grain size and DRX volume fraction in the TUSF specimen (Figure 18b), attributed to the uneven distribution of grain size and DRX during drawing.

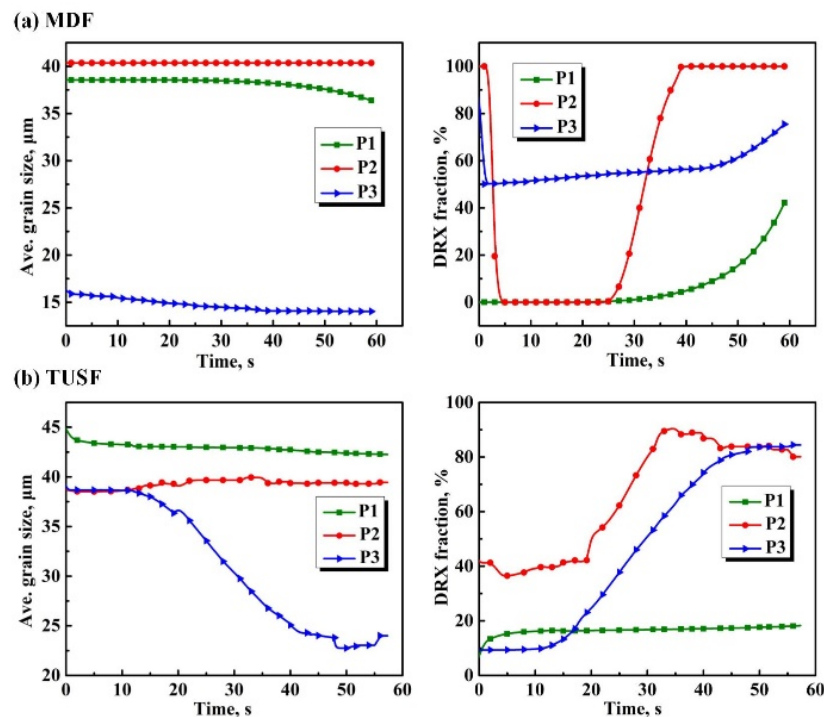


**Figure 18.** Time-dependent average grain size and DRX fraction curves for (a) MDF and (b) TUSF specimens at different tracking points.

## 6. Conclusions

- (1) The grain size distribution in the MDF specimen was inhomogeneous. During the first step of MDF, the microstructure undergoes significant grain refinement, but an inhomogeneous grain structure was obtained due to the inhomogeneous strain distribution at the centre and edge regions. Finer grains developed at the centre region during forging. Based on experimental results, the microstructural evolutionary model used in this study is reliable;
- (2) The forged ingot had an inhomogeneous grain distribution, and the average grain size at the core of the SDP1 steel sample after MDF was approximately 40.6–43.3  $\mu\text{m}$ . Although this was slightly greater than the post-TUSF grain size (35.7–46.0  $\mu\text{m}$ ), the microstructure of the SDP1 steel sample after MDF was more uniform than that after TUSF;
- (3) After MDF, the grains at the core of the sample were completely recrystallised (a recrystallisation volume fraction of 100%). In contrast, after TUSF, the grains at the centre of the sample were completely recrystallised, resulting in a nonuniform grain structure. Insufficient recrystallisation can result in mixed crystals;
- (4) The average grain size of the SDP1 steel sample after MDF was 11.0–60.0  $\mu\text{m}$ , which was smaller than that of the post-TUSF sample (12.0–132.0  $\mu\text{m}$ ). In addition, the surface of the sample after TUSF was not smooth, which can affect the overall performance of the sample and subsequent processing.

**Author Contributions:** Conceptualisation, X.C. and J.L. (Junwan Li); methodology, X.Z.; software, X.Z.; validation, X.C., B.W. and J.L. (Jiayuan Li); formal analysis, X.C.; investigation, X.C.; resources, X.W.; data curation, B.W.; writing—original draft preparation, X.C. and X.Z.; writing—review and editing, J.L. (Junwan Li) and P.Z.; visualisation, X.C.; supervision, J.L. (Junwan Li); project administration, X.C.; funding acquisition, X.W. All authors have read and agreed to the published version of the manuscript.

**Funding:** This research was funded by National Key R&D Program of China (grant numbers: 2016YFB0300400 and 2016YFB0300404).

**Data Availability Statement:** The data presented in this study are available upon request from the corresponding author. The data are not publicly available due to the fact of technical or time limitations.

**Acknowledgments:** The authors are grateful to Xiaocheng Li., Xijuan He. and Jie Ji. for their contribution to the discussion.

**Conflicts of Interest:** The authors declare no conflict of interest.

## References

1. Zheng, Y.-F.; Wu, R.-M.; Li, X.-C.; Wu, X.-C. Continuous cooling transformation behaviour and bainite formation kinetics of new bainitic steel. *Mater. Sci. Technol.* **2016**, *33*, 454–463. [[CrossRef](#)]
2. Wu, R.M.; Zheng, Y.; Wu, X.C.; Li, X.C. Effect of titanium on the microstructure and hardness uniformity of non-quenched and tempered prehardened steel for large-section plastic mould. *Ironmak. Steelmak.* **2016**, *44*, 17–22. [[CrossRef](#)]
3. Xiaoxiao, Z.; Xuan, C.; Xiaocheng, L.; Yushu, H.; Junwan, L.; Xiaochun, W. Numerical Study on Microstructure Evolution of Large Cross-section SDP1 Plastic Die Steel during Multi-directional Forging. *Shanghai Metals* **2020**, *42*, 57–62. [[CrossRef](#)]
4. Xiao, Z.; Yang, X.; Wang, J.; Fang, Z.; Guo, C.; Zhang, D.; Yang, Y.; Zhang, X. Influence of Fe addition on annealing behaviors of a phosphorus containing brass. *J. Alloys. Compd.* **2017**, *712*, 268–276. [[CrossRef](#)]
5. Tang, L.; Liu, C.; Chen, Z.; Ji, D.; Xiao, H. Microstructures and tensile properties of Mg–Gd–Y–Zr alloy during multidirectional forging at 773K. *Mater. Des.* **2013**, *50*, 587–596. [[CrossRef](#)]
6. Bahmani, A.; Arthanari, S.; Shin, K.S. Achieving a high corrosion resistant and high strength magnesium alloy using multi directional forging. *J. Alloys Compd.* **2020**, *856*, 158077. [[CrossRef](#)]
7. Heidarzadeh, A.; Saeid, T.; Klemm, V. Microstructure, texture, and mechanical properties of friction stir welded commercial brass alloy. *Mater. Charact.* **2016**, *119*, 84–91. [[CrossRef](#)]
8. Miura, H.; Yu, G.; Yang, X. Multi-directional forging of AZ61Mg alloy under decreasing temperature conditions and improvement of its mechanical properties. *Mat. Sci. Eng. A-Struct.* **2011**, *528*, 6981–6992. [[CrossRef](#)]
9. Zherebtsov, S.V.; Salishchev, G.A.; Galeyev, R.M.; Valiakhmetov, O.R.; Mironov, S.Y.; Semiatin, S.L. Production of submicrocrystalline structure in large-scale Ti–6Al–4V billet by warm severe deformation processing. *Scripta Mater.* **2004**, *51*, 1147–1151. [[CrossRef](#)]
10. Miura, H.; Maruoka, T.; Yang, X.; Jonas, J.J. Microstructure and mechanical properties of multi-directionally forged Mg–Al–Zn alloy. *Scripta Mater.* **2012**, *66*, 49–51. [[CrossRef](#)]
11. Gubicza, J.; Dobatkin, S.; Khosravi, E.; Kuznetsov, A.; Lábár, J.L. Microstructural stability of Cu processed by different routes of severe plastic deformation. *Mater. Sci. Eng. A* **2011**, *528*, 1828–1832. [[CrossRef](#)]
12. Sitdikov, O.; Sakai, T.; Miura, H.; Hama, C. Temperature effect on fine-grained structure formation in high-strength Al alloy 7475 during hot severe deformation. *Mater. Sci. Eng. A* **2009**, *516*, 180–188. [[CrossRef](#)]
13. Nunes, L.G.d.S.; Machado, M.L.P. Simulation of the Accumulative Roll-Bonding process through warm torsion test. *J. Mater. Res. Technol.* **2018**, *7*, 326–330. [[CrossRef](#)]
14. Wang, H.; Su, L.; Yu, H.; Lu, C.; Tieu, A.K.; Liu, Y.; Zhang, J. A new finite element model for multi-cycle accumulative roll-bonding process and experiment verification. *Mater. Sci. Eng. A-Struct.* **2018**, *726*, 93–101. [[CrossRef](#)]
15. Kulagin, R.; Beygelzimer, Y.; Ivanisenko, Y.; Mazilkin, A.; Straumal, B.; Hahn, H. Instabilities of interfaces between dissimilar metals induced by high pressure torsion. *Mater. Lett.* **2018**, *222*, 172–175. [[CrossRef](#)]
16. Li, P.; Lin, Q.; Wang, X.; Tian, Y.; Xue, K.-M. Recrystallization behavior of pure molybdenum powder processed by high-pressure torsion. *Int. J. Refract. Met. Hard Mater.* **2018**, *72*, 367–372. [[CrossRef](#)]
17. Martynenko, N.; Lukyanova, E.; Serebryany, V.; Gorshenkov, M.; Shchetinin, I.; Raab, G.; Dobatkin, S.; Estrin, Y. Increasing strength and ductility of magnesium alloy WE43 by equal-channel angular pressing. *Mater. Sci. Eng. A-Struct.* **2018**, *712*, 625–629. [[CrossRef](#)]
18. Wei, J.; You, J.; Zhang, D.; Jiang, S.; Chen, Z.; Liu, C. Reducing yield asymmetry in a wrought Mg–9Al alloy by randomized texture achieved via multi-directional forging. *Mat. Sci. Eng. A-Struct.* **2020**, *796*, 140003. [[CrossRef](#)]
19. Manjunath, G.A.; Shivakumar, S.; Fernandez, R.; Nikhil, R.; Sharath, P.C. A review on effect of multi-directional forging/multi-axial forging on mechanical and microstructural properties of aluminum alloy. *Mater. Today. Proc.* **2021**, *47*, 2565–2569. [[CrossRef](#)]
20. Bagherpour, E.; Pardis, N.; Reihanian, M.; Ebrahimi, R. An overview on severe plastic deformation: Research status, techniques classification, microstructure evolution, and applications. *Int. J. Adv. Manuf. Technol.* **2018**, *100*, 1647–1694. [[CrossRef](#)]
21. Xing, J.; Yang, X.; Miura, H.; Sakai, T. Mechanical Properties of Magnesium Alloy AZ31 after Severe Plastic Deformation. *Mater. Trans.* **2008**, *49*, 69–75. [[CrossRef](#)]
22. Zhang, R.; Wang, D.; Yuan, S. Effect of multi-directional forging on the microstructure and mechanical properties of TiBw/TA15 composite with network architecture. *Mater. Des.* **2017**, *134*, 250–258. [[CrossRef](#)]
23. Zhang, Z.; Qu, S.; Feng, A.; Shen, J. Achieving grain refinement and enhanced mechanical properties in Ti–6Al–4V alloy produced by multidirectional isothermal forging. *Mater. Sci. Eng. A-Struct.* **2017**, *692*, 127–138. [[CrossRef](#)]
24. Khani Moghanaki, S.; Kazeminezhad, M.; Logé, R. Mechanical behavior and texture development of over-aged and solution treated Al–Cu–Mg alloy during multi-directional forging. *Mater. Charact.* **2018**, *135*, 221–227. [[CrossRef](#)]

25. Huang, H.; Zhang, J. Microstructure and mechanical properties of AZ31 magnesium alloy processed by multi-directional forging at different temperatures. *Mater. Sci. Eng. A-Struct.* **2016**, *674*, 52–58. [[CrossRef](#)]
26. Seshacharyulu, T.; Medeiros, S.; Morgan, J.; Malas, J.; Frazier, W.; Prasad, Y. Hot deformation mechanisms in ELI Grade Ti-6Al-4V. *Scr. Mater.* **1999**, *41*, 283–288. [[CrossRef](#)]
27. Nakao, Y.; Miura, H. Nano-grain evolution in austenitic stainless steel during multi-directional forging. *Mater. Sci. Eng. A-Struct.* **2011**, *528*, 1310–1317. [[CrossRef](#)]
28. Zharebtsov, S.; Murzinova, M.; Salishchev, G.; Semiatin, S. Spheroidization of the lamellar microstructure in Ti-6Al-4V alloy during warm deformation and annealing. *Acta Mater.* **2011**, *59*, 4138–4150. [[CrossRef](#)]
29. Soleymani, V.; Eghbali, B. Grain Refinement in a Low Carbon Steel Through Multidirectional Forging. *J. Iron Steel Res. Int.* **2012**, *19*, 74–78. [[CrossRef](#)]
30. Li, X.; Duan, L.; Li, J.; Wu, X. Experimental study and numerical simulation of dynamic recrystallization behavior of a microalloyed plastic mold steel. *Mater. Des.* **2015**, *66*, 309–320. [[CrossRef](#)]
31. Kim, W.J.; Hong, S.I.; Kim, Y.S.; Min, S.H.; Jeong, H.T.; Lee, J.D. Texture development and its effect on mechanical properties of an AZ61 Mg alloy fabricated by equal channel angular pressing. *Acta Mater.* **2003**, *51*, 3293–3307. [[CrossRef](#)]
32. Sakai, T.; Belyakov, A.; Kaibyshev, R.; Miura, H.; Jonas, J.J. Dynamic and post-dynamic recrystallization under hot, cold and severe plastic deformation conditions. *Prog. Mater. Sci.* **2014**, *60*, 130–207. [[CrossRef](#)]
33. Lu, Y.; Ma, R.; Wang, Y.-n. Texture evolution and recrystallization behaviors of Cu–Ag alloys subjected to cryogenic rolling. *T. Nonferr. Metal. Soc.* **2015**, *25*, 2948–2957. [[CrossRef](#)]
34. Dehghan-Manshadi, A.; Barnett, M.R.; Hodgson, P.D. Recrystallization in AISI 304 austenitic stainless steel during and after hot deformation. *Mat. Sci. Eng. A-Struct.* **2008**, *485*, 664–672. [[CrossRef](#)]
35. Montheillet, F.; Lurdos, O.; Damamme, G. A grain scale approach for modeling steady-state discontinuous dynamic recrystallization. *Acta Mater.* **2009**, *57*, 1602–1612. [[CrossRef](#)]
36. Eghbali, B. Effect of strain rate on the microstructural development through continuous dynamic recrystallization in a microalloyed steel. *Mater. Sci. Eng. A-Struct.* **2010**, *527*, 3402–3406. [[CrossRef](#)]
37. Li, D.; Guo, Q.; Guo, S.; Peng, H.; Wu, Z. The microstructure evolution and nucleation mechanisms of dynamic recrystallization in hot-deformed Inconel 625 superalloy. *Mater. Des.* **2011**, *32*, 696–705. [[CrossRef](#)]
38. Vervynckt, S.; Verbeken, K.; Thibaux, P.; Houbaert, Y. Recrystallization–precipitation interaction during austenite hot deformation of a Nb microalloyed steel. *Mat. Sci. Eng. A-Struct.* **2011**, *528*, 5519–5528. [[CrossRef](#)]
39. BadJena, S.; Park, J. Effect of particles on the dynamic recrystallization behavior of Al–V–N microalloyed medium carbon steel. *Mater. Sci. Eng. A-Struct.* **2012**, *548*, 126–133. [[CrossRef](#)]
40. Mehtonen, S.; Karjalainen, L.; Porter, D. Hot deformation behavior and microstructure evolution of a stabilized high-Cr ferritic stainless steel. *Mater. Sci. Eng. A-Struct.* **2013**, *571*, 1–12. [[CrossRef](#)]